

Residual Stresses in Inertia-Friction-Welded Dissimilar High-Strength Steels

R.J. MOAT, D.J. HUGHES, A. STEUWER, N. IQBAL, M. PREUSS, S.E. BRAY,
and M. RAWSON

The welding of dissimilar alloys is seen increasingly as a way forward to improve efficiencies in modern aeroengines, because it allows one to tailor varying material property demands across a component. Dissimilar inertia friction welding (IFW) of two high-strength steels, Aermet 100 and S/CMV, has been identified as a possible joint for rotating gas turbine components and the resulting welds are investigated in this article. In order to understand the impact of the welding process and predict the life expectancy of such structures, a detailed understanding of the residual stress fields present in the welded component is needed. By combining energy-dispersive synchrotron X-ray diffraction (EDSXR) and neutron diffraction, it has been possible to map the variations in lattice spacing of the ferritic phase on both sides of two tubular Aermet 100-S/CMV inertia friction welds (as-welded and postweld heat-treated condition) with a wall thickness of 37 mm. Laboratory-based XRD measurements were required to take into account the variation in the strain-free d -spacing across the weld region. It was found that, in the heat-affected zone (HAZ) slightly away from the weld line, residual stress fields showed tensile stresses increasing most dramatically in the hoop direction toward the weld line. Closer to the weld line, in the plastically affected zone, a sharp drop in the residual stresses was observed on both sides, although more dramatically in the S/CMV. In addition to residual stress mapping, synchrotron XRD measurements were carried out to map microstructural changes in thin slices cut from the welds. By studying the diffraction peak asymmetry of the 200- α diffraction peak, it was possible to demonstrate that a martensitic phase transformation in the S/CMV is responsible for the significant stress reduction close to the weld line. The postweld heat treatment (PWHT) chosen to avoid any overaging of the Aermet 100 and to temper the S/CMV martensite resulted in little stress relief on the S/CMV side of the weld.

DOI: 10.1007/s11661-009-9915-0

© The Minerals, Metals & Materials Society and ASM International 2009

I. INTRODUCTION

THERE is a constant drive within the aerospace industry to increase the efficiency of the engines being produced, for both economic and environmental reasons. One possibility for improving the efficiency is to reduce the weight and size of the engine components, which requires the tailoring of the materials' properties across a component. In the present study, inertia friction welding (IFW) has been used to join Aermet 100, a very high-strength and high-toughness secondary-hardening steel, and S/CMV, a high-strength, heat-resistant, Cr-Mo pressure vessel steel. This design might enable the production of rotating gas turbine components that

can withstand very high torsional forces on the one end (Aermet 100) and exhibit sufficient properties at temperatures of several hundred degrees Celsius on the other end (S/CMV) of the component.^[1,2]

The fundamental principle of friction welding is to use the heat generated through motional friction to produce a clean joint, without the formation of a liquid phase.^[3] The IFW involves using energy stored in a flywheel to rotate one-half of a component while the second half is forced into contact. This contact force first generates heat at the interface. Once the material has become sufficiently soft, the forging pressure applied against the two components forces the heated interface material into the flash, removing any surface contaminants and producing a clean joint.^[3] Due to the rotational aspect of the process, IFW is particularly suited to welding cylindrical parts. The solid-state nature opens opportunities for joining materials previously considered to be unweldable and dissimilar materials. To date, only a small number of reports regarding dissimilar IFW are available in the public domain, with articles reporting the analysis of dissimilar Cr-Mo steels,^[4] dissimilar stainless steels,^[5] stainless steel and titanium,^[6] dissimilar nickel superalloys,^[7-9] and the steels welded in this study.^[2,10,11] The joining

R.J. MOAT, N. IQBAL, and M. PREUSS are with the School of Materials, University of Manchester, Manchester, M1 7HS, United Kingdom. Contact e-mail: richard.moat@manchester.ac.uk D.J. HUGHES is with the Institute Laue-Langevin, 38042 Grenoble Cedex-9, France. A. STEUWER, formerly with the FaME38 at the Institut Laue-Langevin/European Synchrotron Radiation Facility (ILL/ESRF), is with the European Spallation Source (ESS) Scandinavia, University of Lund, 22350 Lund, Sweden. S.E. BRAY and M. RAWSON are with Rolls-Royce plc, Derby, DB24 8BJ, United Kingdom.

Manuscript submitted September 25, 2008.

Article published online July 24, 2009

of dissimilar materials by fusion welding is often hampered by the formation of undesirable brittle phases during solidification and significant differences in the melting points between the two materials to be joined. In the case of IFW, the intermetallic phase formation when joining aluminum alloys to steel can still be a problem^[12] but, due to the absence of a liquid phase and, in some cases, extremely short welding times, these issues can be minimized. When joining different materials by inertia friction, high-temperature mechanical properties also present a challenge. This is particularly the case when joining structural components, because deformation on both sides of the weld line will provide a self-cleaning process at the weld interface, ensuring a joint. Even without melt-phase formation during IFW, the components experience severe levels of plastic deformation in the weld region and high thermal gradients across the weld line, both causing significant microstructural variations and residual stress formation. Two main microstructural regions are formed during IFW: a thermomechanically affected zone (TMAZ) very near the weld line, which is affected by deformation and thermal changes, and a heat-affected zone (HAZ) slightly further away from the weld line, which is affected only by thermal changes.^[13]

A limited amount of work has been reported on the characterization of residual stresses in IFW components. Most of the studies so far have focused on the welding of tubular components of nickel-base superalloys with a wall thickness less than 10 mm.^[14–17] In such IFWs, the largest tensile stresses are observed in the hoop direction, very close to the weld line near the inner diameter (ID), while the lowest stresses are generally observed in the radial direction. In the axial direction, a bending moment is observed, which is most likely the product of a tourniquet effect from the dominant hoop stresses.^[18] Substantial efforts have been made by the power generation industry to understand and control the residual stresses generated when welding steel components. A review of the residual stresses in ferritic power plant steel-fusion welds can be found in Reference 19; this outlines how the martensite phase transformation can result in a change from tensile stresses to compressive stresses within the weld zone due to the associated volume increase in the martensite. The volume change that is experienced during the austenite-to-martensite phase transformation is permanent. During welding, this volume change can be accommodated through relief of the tensile stresses forming due to thermal expansion; however, if the transformation strain is sufficient, stresses can become compressive. Previous work carried out on S/CMV-Aermet 100 inertia friction welds^[2] has indicated that martensite forms in these weldments.

The present article reports the residual stress development in two inertia-friction-welded Aermet 100 and S/CMV tubular components (as-welded and postweld heat-treated condition). In addition, the results of the microstructural mapping of retained austenite, identification of martensitically transformed regions, and Vickers hardness mapping are presented here, to enable a discussion of the observed residual stress fields in terms of the martensitic phase transformation. Due to the large wall thickness of the studied welds (37 mm), it was important to characterize the microstructure of the welds not only across the weld line but also as a function of the radial position. The residual strain mapping of such large wall-thickness welds in combination with a relatively small outside diameter (approximately 132 mm) presented a particular challenge and required the combination of energy-dispersive synchrotron X-ray diffraction (EDSXR) and neutron diffraction. In conjunction with these measurements, laboratory-based XRD was used to apply a strain-free lattice parameter (d_0) correction, accounting for the effect of microstructural/chemistry changes across the weld line.

II. MATERIALS

Because the microstructural evolution across the weld line is expected to have a significant impact on the residual stress development, an understanding of the materials is essential. Aermet 100 is an age-hardening Ni-Co-Mo steel^[20] consisting of a dual-phase ferrite/austenite (optimum 7 to 9 pct austenite) structure.^[21] The chemical composition of the alloy can be found in Table I. Due to the relatively high levels of γ stabilizers, the martensite finish temperature of Aermet 100 is below room temperature. Consequently, when quenched in oil, increased levels of retained austenite are present. The exceptional mechanical properties of the Aermet 100 (tensile strength close to 1.8 GPa and toughness better than 170 MPa \sqrt{m}) are achieved by aging the quenched material at a temperature below 500 °C, resulting in the precipitation of very fine molybdenum-rich M₂C carbides, which are coherent in the matrix, and thin austenite films. When aging Aermet 100 at higher temperatures, these exceptional mechanical properties are quickly lost due to overaging, giving this alloy a very narrow heat-treatment window for aging.^[22–24] To reduce the effect of overaging during postweld heat treatment (PWHT), Aermet 100 can be joined in a partially aged condition.

The S/CMV is a low-alloy, Cr-Mo steel similar to type EN40C, used for pressure vessel applications (Table I for chemical composition). The S/CMV does not exhibit

Table I. Nominal Composition of Aermet 100 and S/CMV

	Element (Wt Pct)									
	C	Cr	Ni	Co	Mo	V	Si	Nb	Mn	Fe
Aermet 100	0.20	2.50	10.10	12.70	1.37	—	—	3.26	0.01	bal
S/CMV	0.30	3.15	—	—	1.60	0.10	0.60	—	—	bal

a secondary aging phenomenon and, therefore, is less sensitive when annealed. With respect to subjecting the S/CMV to IFW, rapid cooling in the weld region is expected to result in martensitic phase transformation, which will have an effect on the mechanical properties and residual stresses through reduced fracture toughness and transformation strain, respectively.

III. EXPERIMENTAL

A. Materials and Specimens

The Aermet 100-S/CMV joints were produced by Rolls-Royce plc (Derby, United Kingdom) using an MTI inertia friction welder. Welds were produced with a finish machined outer diameter (OD) of 132 mm and an ID of 58 mm, using partially aged Aermet 100 and fully heat-treated S/CMV. Two welds were produced, using identical welding parameters. Weld 1 was kept in the as-welded condition, while weld 2 received a tempering PWHT in a regime that retained maximum strength and toughness in Aermet 100.

After welding and machining, the windows were spark eroded to allow passage of the incident synchrotron

X-ray beams (Figure 1). The material removed from these windows was retained and used for microhardness, d_0 measurement, and synchrotron XRD microstructural mapping. Further windows were machined after the EDSXRD measurements had been completed, to allow the passage of incident and diffracted neutron beams to determine the radial strains near the ID of the tubular-shaped welds (Figure 2). Because the windows were kept as small as possible and were far away from the point of the measurements, it can be assumed that they did not affect the residual stress field.

B. Vickers Microhardness

Microhardness mapping was performed on a calibrated Vickers Hardness indenter (OmniMet MHT Automatic Microhardness Testing System)* with auto-

*OmniMet MHT Automatic Microhardness Testing System is a registered trademark of Buehler Ltd, Lake Bluff, IL.

mated stage- and indent-measuring software. Measurements were performed on the material removed for the

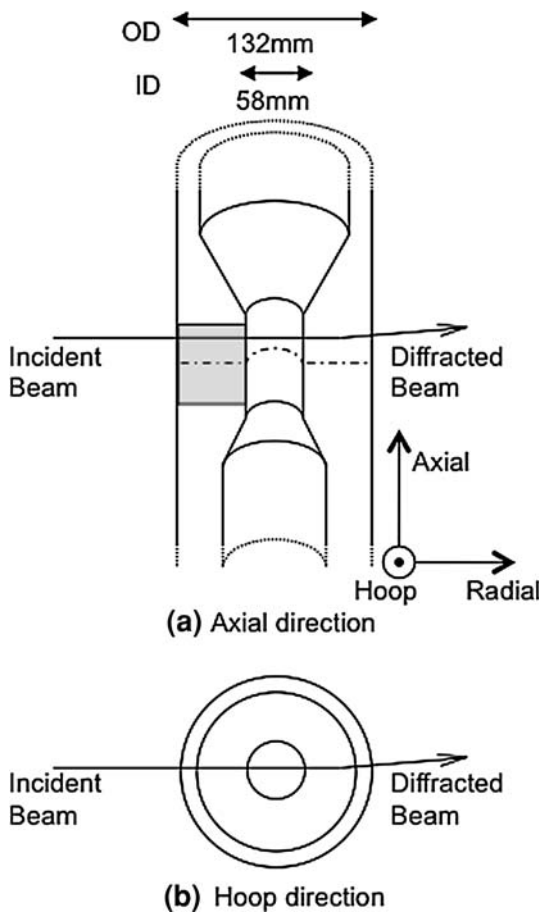


Fig. 1—Schematic of the setup used at ID15 to measure axial and hoop strain simultaneously (shaded areas indicating windows machined into samples).

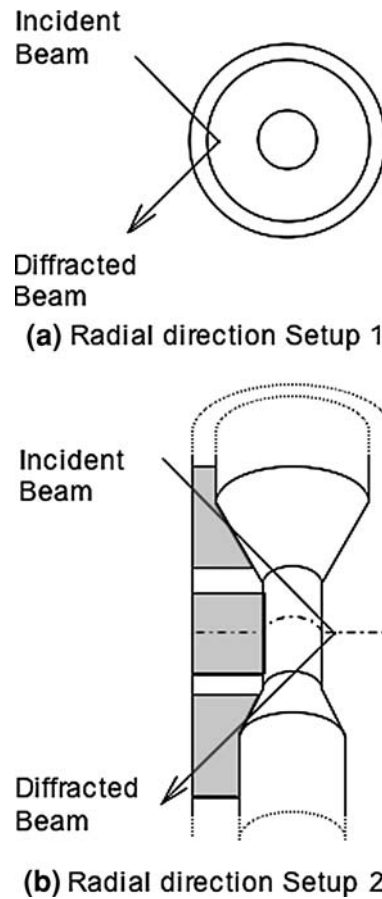


Fig. 2—Schematic of the two setups used at SALSA to measure the radial strains (a) near the OD and in the center and (b) near the ID (shaded areas indicating windows machined into samples).

EDSXR measurements, ground, polished, and sufficiently etched, using 2 pct nital etchant, to reveal the weld line. In general, the samples were underetched, in order to avoid problems when measuring the size of the indent using the image-analysis software. Indents were placed with a step size of 1 mm in the axial direction and 7.4 mm in the radial direction.

C. Axial and Hoop Strain Measurements Using EDSXR

The hoop and axial strain directions (Figure 1 for direction definitions) were measured using EDSXR on the high-energy beam line ID15A at the European Synchrotron Radiation Facility (ESRF) (Grenoble, France).^[25] This beam line can be operated in white-beam mode, with a pair of energy-sensitive Ge detectors positioned such that two orthogonal strain directions can be collected simultaneously. This setup allows for full diffraction patterns to be collected using energies ranging from 60 to 300 KeV.^[25] By analyzing multiple peak spectra, errors emanating from the texture, intergranular strains, and anisotropy are minimized.

High-energy X-rays are required to achieve sufficient penetration through the weld wall and measure residual strains deep inside the component. Consequently, the diffraction angle is low and the setup for this experiment used a 2θ angle of 5 deg. With a diffraction angle this low, it was geometrically unfeasible to measure the radial direction using EDSXR (Figure 1). Therefore, this direction was measured using neutron diffraction. It should be noted that the two strain vectors measured in the EDSXR setup oriented 2.5 deg away from the true axial and hoop directions, but the variation in strain caused by this small deviation is assumed to be negligible.^[26]

The experimental data were analyzed using the General Structure Analysis System (GSAS) fitting package^[27,28] to perform a Rietveld analysis on the EDSXR data. The positioning matrix used for microhardness mapping was also applied for these measurements. A slit-defined beam of $340 \times 340 \mu\text{m}$ was used, resulting in a gage volume length of approximately 7.4 mm in the radial direction. This was the largest possible gage volume to be fully submerged within the sample without overlap in the radial direction and gaining sufficient diffraction peak statistics in a reasonable time scale. Counting times of 5 minutes per measurement point were necessary to obtain strain accuracies better than the 6×10^{-5} lattice strain.

D. Radial Strain Measurements Using Neutron Diffraction

Neutron diffraction gives the possibility of high-depth penetrations at large diffraction angles (an angle of 90 deg is often desirable). This is achieved by utilizing relatively high-wavelength neutrons, which, unlike X-rays, do not sacrifice penetration depth. This has been notably exploited by Edwards *et al.* in thick-section steel cylinders with a geometry similar to those studied in this manuscript.^[29] Due to the tubular geometry and the

thickness of the walls, two experimental setups were employed: one to measure the radial strains near the OD and in the center (Figure 2(a)) and one to measure the radial strains near the ID (Figure 2(b)).

The two distinct sets of measurements were performed on the strain-imaging beam line SALSA^[30] at the Institut Laue-Langevin (ILL) (Grenoble, France) using a monochromatic 1.6-Å wavelength neutron beam allowing for the ferrite 211 diffraction peak to be analyzed at a 2θ angle of ~85 deg. Data were analyzed by fitting the diffraction peaks to a single Gaussian peak with a flat background. The beam was slit defined, resulting in an approximate gage volume of $4 \times 4 \times 3$ mm (horizontal-incident \times horizontal-receiving \times vertical) for the first setup (Figure 2(a)) and $7 \times 3 \times 3$ mm (horizontal-incident \times horizontal-receiving \times vertical) for the second setup (Figure 2(b)). With gage volumes of these sizes, counting times ranging from 5 to 35 minutes were employed, depending on the neutron path length.

E. Microstructural Mapping Using Monochromatic Synchrotron XRD

Monochromatic transmission synchrotron XRD was used to map the retained austenite phase fraction and peak asymmetry across the welds. The measurements were carried out using slit-defined, monochromatic X-ray radiation of 80 KeV on the materials science beam line ID11 at the ESRF. The samples were mounted in such a way that the beam was parallel to the radial direction, allowing mapping of the sample in the axial and hoop directions. Debye-Scherrer rings were recorded at a distance of 222 mm from the sample using a two-dimensional (2-D) FRELON-type area detector, an in-house detector of the ESRF, Grenoble, France.

The diffraction rings observed in 2-D diffraction images were integrated over an angular range of 360 deg using Fit2D^[31] and analyzed to obtain the austenite volume fraction and ferrite 200 peak asymmetry. The austenite fraction was analyzed using pseudo-Voigt peak fitting and calculations based on the ASTM standard for phase fraction determination.^[32] By using an area detector and an average of approximately 360 deg, the effect of nonrandom texture can be reduced. Due to very similar peak positions of the ferritic and martensitic diffraction peaks in low-carbon steels, it was impossible to deconvolute the diffraction peaks of the two phases. In order to identify regions of possible martensitic phase transformation, the asymmetry of the 200 ferrite peak was analyzed, giving a qualitative indication of the presence of a martensite peak, slightly offset from the ferrite peak. The asymmetry was analyzed using a Fraser-Suzuki-modified Gaussian equation.^[33]

F. Laboratory-Based XRD

In welds of engineering alloys, which are sensitive to the temperatures reached, it can generally be assumed that the chemistry of the individual phases will change due to the thermal history the material has undergone during welding. Consequently, the strain-free d -spacing

of a phase will change across the HAZ of a weld, which is important to consider when measuring residual strains in the way described earlier. Measurements to determine such d_0 variations were carried out using a laboratory X-ray diffractometer. By assuming that the stress normal to an unstrained surface is zero, combined with the characteristic low penetration of lab X-rays in crystalline metals, the d_0 can be calculated using the $\sin^2\psi$ method. A more detailed explanation of the method can be found in References 34 and 35. The diffractometer used for the present study was a Bruker AXS D8 Discover equipped with a chromium anode X-ray tube emitting radiation of wavelength 2.2909 Å and an area detector collecting backscattered X-rays from the (211) Debye–Scherrer diffraction cone at an approximate diffraction angle of ~155 deg. This diffractometer is fitted with a laser and optical video microscope, which enables one to accurately align the sample for each measurement point. Each measurement point was collected over 4 hours with an irradiated area of approximately 1 mm². As mentioned earlier, measurements were carried out on the slices cut from the welds. Data were recorded using the same position matrix as during the synchrotron XRD and neutron diffraction experiment, mapping the radial and axial variation of the strain-free d -spacing.

G. Stress Calculations

In order to calculate triaxial residual stress, the strain must first be determined in these three directions. The strain is calculated using

$$\varepsilon = \frac{d - d_0}{d_0} = \frac{a - a_0}{a_0} \quad [1]$$

where d and a are the measured d -spacing and lattice parameter, respectively, and d_0 and a_0 are the strain-free d -spacing and lattice parameter. The d -spacing is calculated from the single-peak measurements on SALSA, while a lattice parameter is extracted from the Rietveld analysis of the ID15 spectra. For this reason, the two respective equations are used for each of the two setups. When taking into account the stress-free lattice spacing variations, Eq. [1] is converted to

$$\varepsilon = \frac{d - (d_0 \times c(R, z))}{(d_0 \times c(R, z))} = \frac{a - (a_0 \times c(R, z))}{(a_0 \times c(R, z))} \quad [2]$$

where $c(R, z)$ is the correction factor as a function of the radial (R) and axial (z) position.

For each of the three directions, residual stress fields were calculated using for example for the axial stress direction:

$$\sigma_{\text{axial}} = \frac{E}{(1 + \nu)(1 - 2\nu)} \times [(1 - \nu)\varepsilon_{\text{axial}} + \nu(\varepsilon_{\text{radial}} + \varepsilon_{\text{hoop}})], \text{ etc.} \quad [3]$$

where E is the Young's modulus and ν is the Poisson's ratio. For diffraction experiments yielding full-spectra data, such as those obtained from the ID15, a bulk value for E and ν can reliably be used. When using a single diffraction peak to determine the strain and stress, such as during the experiment on SALSA, the reflection-specific diffraction elastic constant should be selected. Because in the current case the residual stresses are calculated using strains measured from a combination of single-peak and Rietveld analysis, it was decided to use the bulk values of $E = 187$ GPa and $\nu = 0.28$ and $E = 208$ GPa and $\nu = 0.27$ for the Aermet 100 and S/CMV, respectively. This should be a reasonable compromise, because Pang *et al.*^[36] reported a less than 8 pct variation in the elastic response between the 211 ferrite peak and the bulk elastic values in high-strength steels during *in-situ* loading on a neutron diffraction beam line. The authors also identified the 211 diffraction as the one least affected by intergranular strain.

In dissimilar welds, measurements very near the weld line can be affected by the diffracting gage volume cutting across both materials. In the current case, no double diffraction peaks were observed in such regions, which would have possibly enabled the deconvolution of the contributions from each side of the weld line. Instead, large lattice parameter variations were measured, which were a result of the two alloys contributing to one diffracting gage volume. Consequently, measurements affected by this were not considered here.

Ideally, stresses should be calculated from measurements of a single calibrated instrument but, as explained earlier, the ID15A measurements had to be combined with measurements from SALSA to calculate the stress fields. In order to validate that the stress fields calculated in this way can be correct, the lattice spacing measurements of the base material were compared for both the SALSA and ID15A data. Because the components measured are a dissimilar weld, the parent material on each side of the weld has a different d -spacing/lattice parameter. In Table II, the lattice parameters for the two parent materials measured using EDSXRD, neutron diffraction, and laboratory X-ray are shown, along

Table II. Lattice Parameters and Effective Strains Calculated for Aermet 100 and S/CMV in the As-Welded Condition for Each of the Instruments Used

	Lattice Parameter for Each Instrument			
	ID15 Detector 1	ID15 Detector 2	SALSA	Laboratory XRD
Aermet 100 parent	2.88656	2.88644	2.88664	2.88542
S/CMV parent	2.88738	2.88720	2.88753	2.88623
Equivalent microstrain	-282 ± 60	-264 ± 52	-308 ± 41	-280 ± 90

with the associated effective strain between the two parent materials. It is reasonable to measure different lattice parameters for the same material on each instrument, because the absolute calibration of the lattice spacing is very difficult. However, the relative difference in the lattice spacing of the two alloys should be comparable by converting the differences of lattice spacing in strain. The variation in the relative strain between the two alloys did not exceed 5×10^{-5} , a reasonable variation considering that strains of $\pm 3 \times 10^{-3}$ were calculated across the weld for the hoop direction in the as-welded condition.

IV. RESULTS AND DISCUSSION

A. Microhardness

The aim of the microhardness mapping was to identify regions in which a possible martensitic phase transformation can be expected to influence the residual stress field in the weld. Figure 3(a) shows a 2-D microhardness map across the weld line for the as-welded condition. The parent S/CMV exhibits a microhardness of ~ 450 HV and the parent Aermet 100 has a microhardness of ~ 500 HV. A narrow region of very low hardness is measured in the HAZ of S/CMV adjacent to a region of very high microhardness (650 HV) in the TMAZ, which extends up to the weld line. On the Aermet 100 side of the weld, the TMAZ

exhibits microhardness similar to the parent, while in the HAZ, an increase in hardness to 600 HV is measured. All radial positions show a similar microhardness for each axial position, which is in contrast to the work reported in Reference 2, in which a distinct curved microhardness was found near the ID and OD within the TMAZs and HAZs.

After PWHT (Figure 3(b)), the parent material of the S/CMV does not show any significant change in microhardness compared to the as-welded condition, while the microhardness of the Aermet 100 parent material has increased by 100 to ~ 600 HV. The HAZ within S/CMV still shows a hardness trough, while the extremely hard region within the TMAZ has dropped by approximately 100 to ~ 550 HV. The TMAZ of the Aermet 100 displays an increase in microhardness similar to that in the parent material, while the hard region in the HAZ has now dropped by approximately 150 to ~ 450 HV.

Figure 3(a) suggests that, due to the high hardness observed in the TMAZ of the S/CMV, a martensitic phase transformation did take place in this region. In the TMAZ and HAZ of the Aermet 100, no such distinct high-hardness region has been observed, although an increased level of microhardness can be seen between 4 and 7 mm from the weld line. Apart from regions of very high hardness, both 2-D microhardness plots (as-welded and postweld heat-treated condition) indicate significant variations in the microstructure throughout the HAZ and TMAZ. Consequently, variations in the strain-free d -spacing in these regions are to be expected, which will have to be taken into account for accurate stress field determinations. A more detailed correlation between the 2-D microhardness maps and microstructural variations can be found in Reference 2.

B. Austenite and Martensite Mapping

Because high microhardness values cannot be used to uniquely identify regions of martensitic phase transformation, particularly in the heavily deformed TMAZ, microstructural mapping using high-energy monochromatic synchrotron XRD was undertaken on the slices, which were first used for recording the hardness maps. In terms of microstructural changes affecting the residual stress field, emphasis is placed here on the analysis of the retained austenite volume fraction (Figure 4) and peak asymmetry (Figure 5) used as a measure to identify regions in which martensitic phase transformation has taken place. Figure 4 shows that the volume fraction of retained austenite varies over a length scale similar to that of the microhardness measurements in Figure 3. Because the S/CMV contains few austenite-stabilizing elements (Table I), it has no austenite present in the parent material. However, in the TMAZ of the as-welded condition, up to 8 pct of retained austenite has been measured. Because of the low levels of austenite-stabilizing elements in the S/CMV, it is suspected that this is due to the deformation stabilization of the austenite phase.^[37] Aermet 100 contains a volume fraction of ~ 5 pct in the parent material, which rises to a maximum of 10 pct in the TMAZ. Most important from

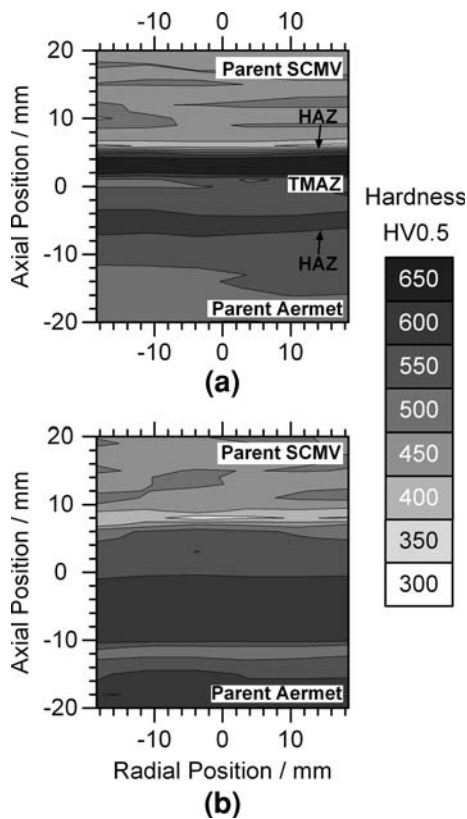


Fig. 3—Vickers microhardness maps of the Aermet 100-S/CMV inertia friction welds in (a) as-welded condition and (b) postweld heat-treated condition.

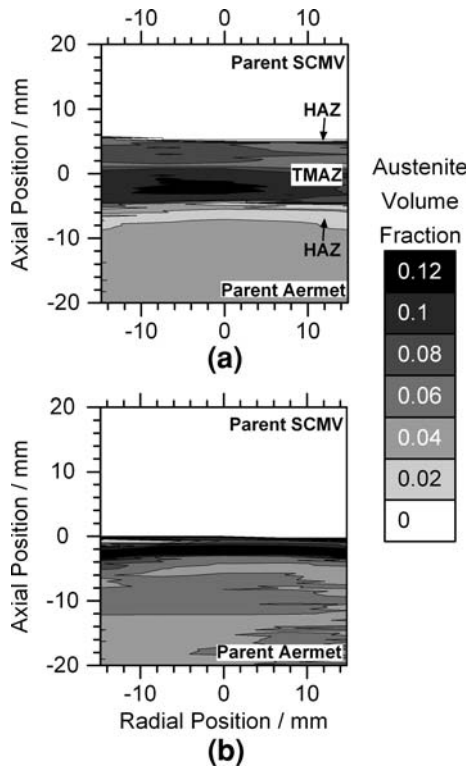


Fig. 4—Austenite volume fraction measured using monochromatic synchrotron XRD for (a) as-welded condition and (b) postweld heat-treated condition.

the residual stress analysis point of view is that, in the parent material, the HAZ and TMAZ of the Aermet 100, the amount of retained austenite is relatively small. For this reason, the residual stress analysis focused exclusively on the dominant ferritic/bainitic/martensitic phases, which allowed reasonably long counting times during the diffraction experiments. Figure 4(b) demonstrates, as one would expect, that, after PWHT, all the retained austenite in the HAZ of the S/CMV has been transformed. On the Aermet 100 side, the amount of retained austenite has increased by approximately 1 pct within all areas. This phenomenon is expected, due to the “precipitation” of stable austenite in secondary-hardening steels.^[22]

The degree of 200 peak asymmetry is plotted in Figure 5, which provides a qualitative indication of regions that have transformed martensitically. In the as-welded condition (Figure 5(a)), a sharp band of asymmetry is measured in the TMAZ of the S/CMV and the HAZ of the Aermet 100. These two regions correspond to the areas of high-hardness levels seen in Figure 3(a). After PWHT, Figure 5(b) shows that no 200 peak asymmetry was detected in the S/CMV, while a thin band of very slight asymmetry is still seen in the HAZ of the Aermet 100. The loss of the 200 peak asymmetry in the TMAZ of the S/CMV corresponds well with a reduction in hardness in this area (Figure 3(b)), which is a result of the martensite being tempered during PWHT. With some slight 200 peak asymmetry still present in the HAZ of the Aermet 100 after PWHT, it has to be assumed that this diffraction

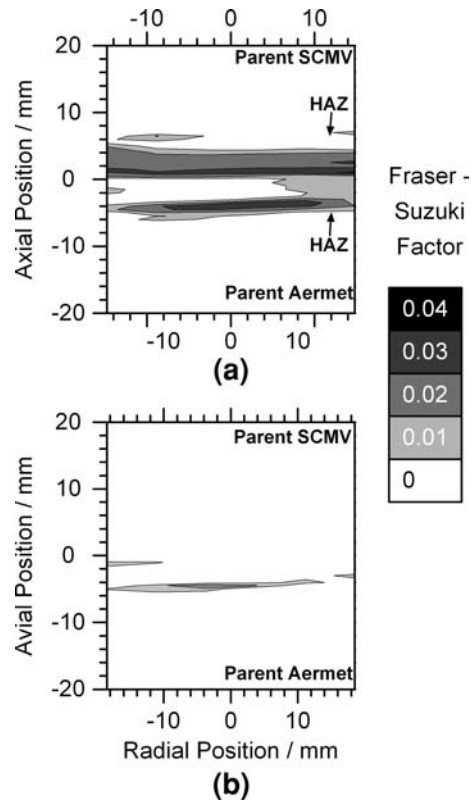


Fig. 5—The 200 diffraction peak asymmetry measured using monochromatic synchrotron XRD of (a) the as-welded condition and (b) postweld heat-treated condition of inertia-friction-welded Aermet 100-S/CMV.

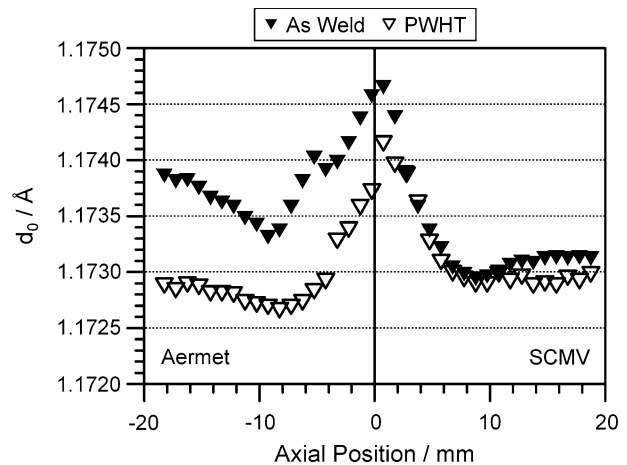


Fig. 6—Variation of strain-free d -spacing measured across the weld line in a thin slice on the (211) diffraction peak at midwall thickness position ($R = 0$ mm).

peak asymmetry is not entirely caused by martensite, because the aging PWHT is expected to be sufficient to fully temper any martensite and age the material.^[20]

C. Strain-Free Lattice Parameter

The variation in the strain-free d -spacing measured on the 211 diffraction peak at midwall thickness across the

weld line is plotted in Figure 6. In the as-welded condition, the Aermet 100 displays a slightly larger $\{211\}$ d_0 -spacing in the base material as compared to the S/CMV. Subjecting the joint to PWHT mainly results in a change in d_0 in the Aermet 100, because this alloy was joined in a partially aged condition and is less thermally stable than the S/CMV. In the S/CMV, only a slight decrease in d_0 spacing can be seen in the parent material. It should be emphasized at this stage that measurement points from very near the weld line (± 2 mm from the weld line) will have covered both sides of the weld, sampling two alloys at the same time. Therefore, measurements from this region were not considered when calculating the correction factors for the d_0 variation (and, consequently, no strain and stress measurements were considered from this region). In both the as-welded and postweld heat-treated condition, an increase in d_0 was measured in the TMAZ. Within the HAZ, a drop in d_0 spacing has been observed on both sides of the weld, which can be attributed to Cr and Mo (both larger than Fe) forming carbides and leaving the ferrite matrix. After PWHT, this drop in d_0 spacing is hardly seen on either side of the HAZ and, at the same time, the d_0 spacing has decreased dramatically in the parent material of the Aermet 100 and slightly in the parent material of the S/CMV. Because the d_0 variation is affected by the thermal history the material was exposed to during welding, Figure 6 also allows one to accurately determine the HAZ of the weld, which is 18 mm in the Aermet 100 and 15 mm in the S/CMV. This measurement of the HAZ extends slightly further than is observed in Figures 3 and 4, which are the measurements of microhardness and retained austenite, respectively. However, the regions of maxima and minima in Figure 6 correlate well with the regions measured in Figures 3 and 4. Correction factors calculated to account for strain-free lattice spacing variations are plotted in Figure 7. These values were subsequently used to correct the d_0 spacing obtained from far-field measurements to take into account the d_0 variation across the weld line.

D. Residual Stresses

To directly compare the effect of the d_0 correction on the residual stresses calculated, plots of the midwall thickness line for the as-welded and postweld heat-treated conditions are presented in Figures 8 and 9, respectively. An average error for the residual stress measurements of ± 45 MPa was calculated from peak fitting uncertainty. Figures 8 and 9 show the hoop stress in the case of using a constant d_0 measured in the far field of the weld and with the d_0 corrected according to Figure 7. For the as-welded condition, the most crucial effect of the d_0 correction is seen in the HAZ of the Aermet 100, where tensile hoop stresses are now calculated after the correction. Within the TMAZ, the increase in d_0 after the correction will result in lower stresses, as compared to assuming a constant strain-free value. This is most significant in the S/CMV, in which, near the weld line, the hoop stresses have become approximately 30 pct more compressive compared to before the d_0 correction. Because of the size of the

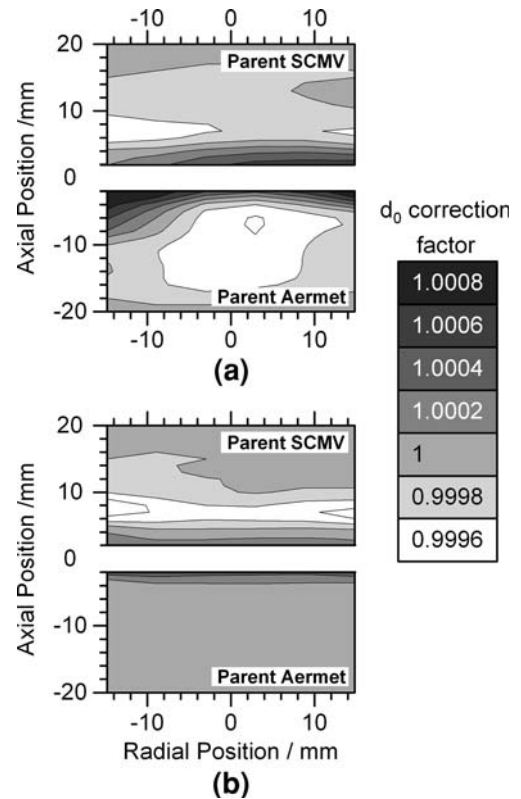


Fig. 7—The d_0 correction factor maps of (a) as-welded condition and (b) postweld heat-treated condition (missing central area is the region with invalid data resulting from the gage volume overlapping the weld line).

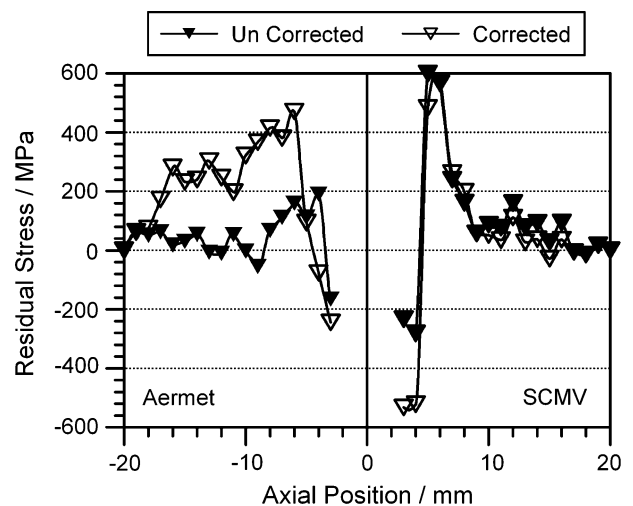


Fig. 8—Comparison of residual hoop stresses in inertia-friction-welded Aermet 100-S/CMV (as welded), calculated at the wall center line with and without d_0 correction (missing data points near the weld line are due to invalid data resulting from the gage volume overlapping the weld line).

diffracting gage volume used during the neutron diffraction measurement, any measurement closer than 2 mm from the weld line resulted in the gage volume cutting across two materials and was not considered for the stress analysis.

Contour plots of the radial, axial, and hoop residual stress fields for the as-welded condition are shown in Figure 10. Large, hoop tensile stresses are measured within the HAZ of the S/CMV, with values of 800 MPa at the ID and OD dropping to 600 MPa at a radial position of 0 mm. Smaller tensile stresses ranging from 100 to 300 MPa are calculated in the other two directions. Tensile stresses are also calculated in the HAZ of the Aermet 100, with stresses up to 450 MPa calculated in the radial and hoop directions and 300 MPa in the axial direction. These stresses show maximum values at the radial center line and approach a stress-free condition toward the ID and OD. Within the TMAZ, stresses range from 0 MPa to maximum compressive stresses of -600 MPa in the hoop direction near the ID and OD. Only in the axial direction in the S/CMV is a tensile stress region observed near the OD.

Figure 11 shows the radial, axial, and hoop residual stresses after PWHT. A region of high tensile stresses mirroring that calculated in the as-welded condition is still found after PWHT in the S/CMV, with little reduction in magnitude (less than 100 MPa). The compressive stresses in the TMAZ of the S/CMV are reduced by the PWHT to a slightly larger extent, with maximum compressive stresses now reaching -400 MPa. In contrast, the PWHT has entirely relieved the tensile stress regions in the HAZ of the Aermet 100 and also reduced the compressive stresses on this side of the weld.

To demonstrate the effect of PWHT more clearly, Figure 12 shows an axial line scan of the d_0 -corrected hoop stresses in the as-welded and postweld heat-treated conditions, at the radial position of 0 mm (the center of the wall thickness). The significant difference in the effectiveness of the PWHT on the two alloys is clear, with a marked stress relief of the postweld heat-treated Aermet 100 and little in the S/CMV. The effect observed is reasonable when the thermal properties of the two steels are taken into account, with the S/CMV being chosen for its thermal stability over the Aermet 100, with an A_{1c} temperature close to 490 °C. Furthermore, the hydrostatic nature of the residual stresses found in the TMAZ will reduce the effectiveness of the PWHT, due to the absence of a deviatoric component.

At this stage, it is worthwhile comparing the residual stress fields presented here with residual stresses observed in other IFW systems. In welds of materials that do not undergo a martensitic phase transformation, the stress formation within the HAZ is mainly governed by the constrained thermal contractions of the weld material during the cooling phase. For example, in inertia-friction-welded nickel-base superalloys with a wall thickness of approximately 10 mm,^[6] tensile hoop stresses rise toward the weld line continuously displaying the highest stresses at the weld line near the ID. In addition, a bending moment of the axial stresses is usually seen in such welds, with tensile axial stresses near the ID and compressive axial stresses near the OD. In the present work, the residual stress distribution is

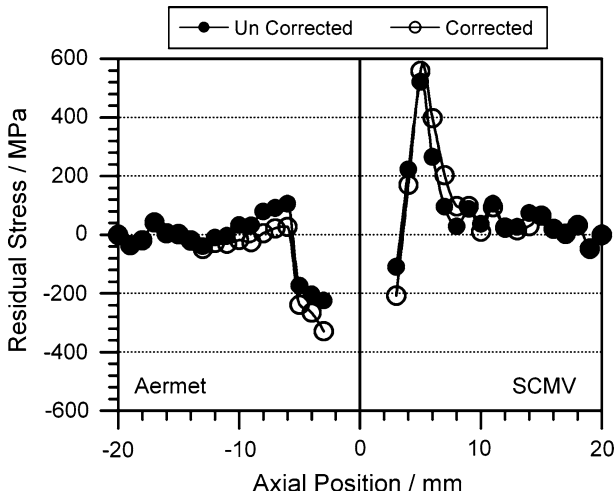


Fig. 9—Comparison of residual hoop stresses in inertia-friction-welded Aermet 100-S/CMV (postweld heat treated) calculated at the wall center line with and without d_0 correction (missing data points near the weld line are due to invalid data resulting from the gage volume overlapping the weld line).

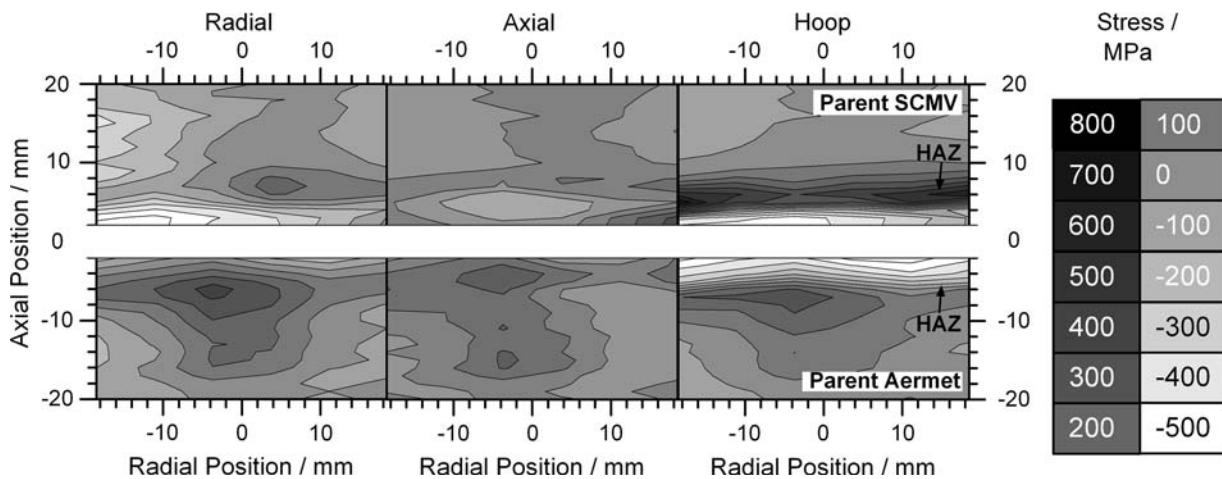


Fig. 10—Residual stress maps for as-welded condition of inertia-friction-welded Aermet 100-S/CMV (missing central area is the region with invalid data resulting from the gage volume overlapping the weld line).

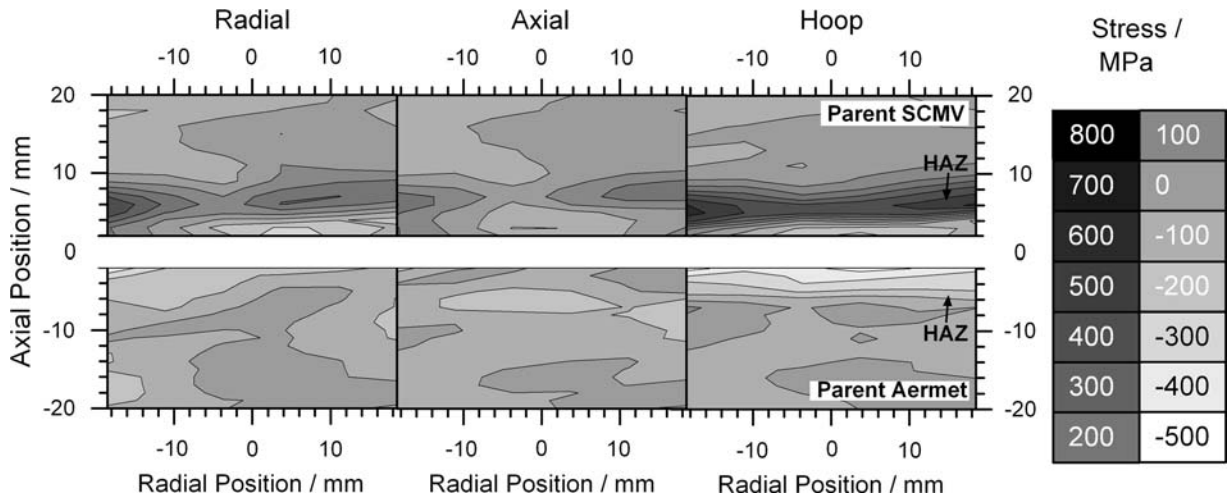


Fig. 11—Residual stress maps for postweld heat-treated condition of inertia-friction-welded Aermet 100-S/CMV (missing central area is region with invalid data resulting from the gage volume overlapping the weld line).

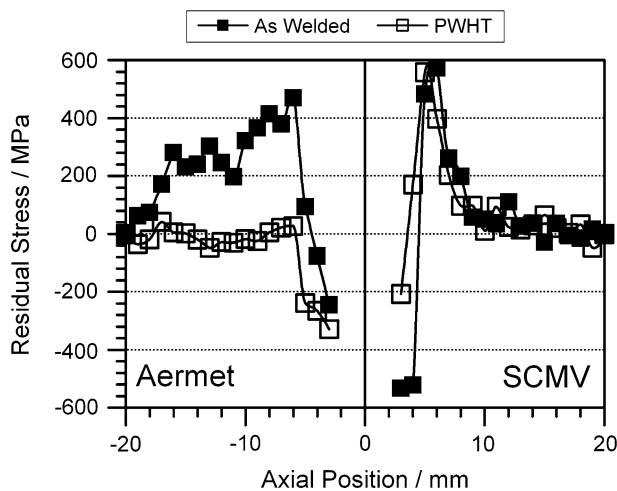


Fig. 12—Comparison of residual hoop stresses of inertia-friction-welded Aermet 100-S/CMV before and after PWHT, calculated at the radial center point (missing data points near the weld line are due to invalid data resulting from the gage volume overlapping the weld line).

considerably different due to the martensitic phase transformation and large wall thickness of the weld. Hoop tensile stresses increase within the HAZ toward the weld line, but then drop into compression in the TMAZ very near the weld line. The reason for the compressive stresses has been confirmed by diffraction peak asymmetry measurements to be a result of a martensitic transformation, similar to that found in the power plant steel fusion welds reviewed in Reference 19. Most important, the largest tensile hoop stresses in the S/CMV are found close to the ID and OD within the HAZ, while the largest compressive hoop stresses were determined in the midwall thickness region very near the weld line. In comparison to the hoop direction, the residual tensile stresses in the axial and radial direction of the S/CMV are significantly smaller. In the Aermet 100, substantial tensile stresses, although slightly smaller

than the peak tensile stresses in the S/CMV, are observed within the HAZ in the radial and hoop direction. Here, the maximum tensile stresses are found in the midwall thickness section while the compressive stresses in the TMAZ tend to be highest more toward the ID and OD. It is worth noting that, compared to the residual stresses reported in Reference 16, stress gradients in the radial and hoop directions are nonmonotonic in the present work. This fundamental difference in the stress field can most likely be attributed to the significantly larger wall thickness of the welds in the present study, as compared to Reference 16. Whereas a thin-wall-thickness inertia friction weld will cool down mainly by having a large heat flux in the axial direction (the parent material acts as a large heat sink), in a large-wall-thickness inertia friction weld, the HAZ is substantially wider and heat loss by radiation becomes more important, resulting in an additional temperature gradient in the radial direction. In addition, it is expected that any clamping forces will have a limited effect on increasing the axial bending moment in such a weld, as reported in Reference 17.

V. SUMMARY AND CONCLUSIONS

The residual stresses in an inertia-welded dissimilar high-strength steel component in the as-welded and postweld heat-treated conditions have been analyzed using a combination of three diffraction techniques. Energy-dispersive XRD and neutron diffraction were used to measure the strain variations across the weld line, while the $\sin^2\psi$ method with laboratory XRD was employed to characterize the variation in the strain-free d -spacing in the HAZ of the weld. Additional microstructure mapping using monochromatic synchrotron X-ray and hardness mapping was undertaken to identify regions of phase transformation relevant for the residual stress generation during welding and to correlate those regions with the residual stress maps. The findings of this work can be summarized as follows.

1. Neutron diffraction, energy-dispersive XRD, and laboratory XRD have successfully been combined to characterize the residual stress field in a tubular weld for possible rotating gas turbine components with a wall thickness of 37 mm. Because of the complex microstructural changes seen across the welds, stress-free lattice spacing analysis was required. Laboratory XRD using the $\sin^2\psi$ method revealed variations in the stress-free lattice parameter in both sides of the weld in the as-welded condition, while in the S/CMV only after PWHT.
2. Largest tensile stresses of approximately 800 MPa were determined in S/CMV in the hoop direction approximately 5 mm from the weld line across the entire radial thickness of the weld.
3. Hydrostatic compressive stresses were calculated in the TMAZ of the S/CMV, which has been attributed to a martensite phase transformation that was identified by microhardness mapping and synchrotron XRD peak asymmetry measurements. Although in the Aermet 100 compressive stresses have only been observed near the weld line in the hoop direction, the radial and axial stresses clearly peak further away from the weld line (in the HAZ) and not right at the weld line. In the region (TMAZ), radial and axial stresses are close to zero. This might be related to a lower activity of martensitic phase transformation during cooling, as indicated by peak asymmetry measurements using synchrotron XRD.
4. The PWHT had limited effect on the stresses in the S/CMV, but was effective in the Aermet 100. Tensile stresses exceeding 800 MPa were still present in the S/CMV after PWHT, which is due to the greater heat resistance properties of the S/CMV compared to the Aermet 100.

ACKNOWLEDGMENTS

The authors acknowledge the provision of beam time from the ILL and ESRF. The authors thank Drs. M. Peel (ID15) and J. Wright (ID11), Messrs. P. Frankel and B. Grant, and Mrs. Judith Shackleton, Manchester Materials Science Center (MMSC) for experimental assistance and the FAME38 project at the ILL for providing hardness-mapping provisions. These experiments were made possible with funding from Rolls Royce plc and the Engineering and Physical Sciences Research Council (Swindon, United Kingdom).

REFERENCES

1. T. Ford: *Aircraft Eng. Aerospace Technol.*, 1997, vol. 69, pp. 555–60.
2. R.J. Moat, M. Karadge, M. Preuss, S. Bray, and M. Rawson: *Mater. Process. Technol.*, 2004, vols. 1–3, pp. 48–58.
3. K.K. Wang: *Weld. Res. Coun. Bull.*, 1974, vol. 204, pp. 1–22.
4. C. Sudha: *J. Nucl. Mater.*, 2002, vol. 302, pp. 193–205.
5. D.G. Lee, K.C. Jang, J.M. Kuk, and I.S. Kim: *J. Mater. Process. Technol.*, 2004, vols. 155–156, pp. 1402–07.
6. Y.C. Kim, A. Fuji, and T.H. North: *Mater. Sci. Technol.*, 1995, vol. 11, pp. 383–87.
7. H.Y. Li, Z.W. Huang, S. Bray, G. Baxter, and P. Bowen: *Mater. Sci. Technol.*, 2007, vol. 23 (12), pp. 1408–18.
8. O. Roder, J. Albrecht, and G. Luterer: *Mater. High Temp.*, 2006, vol. 23 (3–4), pp. 171–77.
9. Z.W. Huang, H.Y. Li, M. Preuss, M. Karadge, P. Bowen, S. Bray, and G. Baxter: *Metall. Mater. Trans. A*, 2007, vol. 38A, pp. 1608–20.
10. C. Bennett, T.H. Hyde, and E.J. Williams: *J. Mater. Des. Appl.*, 2007, vol. 221 (4), pp. 275–84.
11. W.S. Robotham, T.H. Hyde, E.J. Williams, P. Brown, I.R. McColl, and C.J. Kong: *Appl. Mech. Mater.*, 2005, vols. 3–4, pp. 131–38.
12. H. Ochi, K. Ogawa, Y. Yamamoto, and Y. Suga: *Int. J. Offshore Polar Eng.*, 1998, vol. 9 (2), pp. 541–46.
13. M.D. Tumuluru: *Weld. Res. Suppl.*, 1984, vol. 9, pp. 289–94.
14. M. Preuss, L.W.L. Pang, P.J. Withers, and G. Baxter: *Metall. Mater. Trans. A*, 2002, vol. 33A, pp. 3227–34.
15. L. Wang, M. Preuss, P.J. Withers, G. Baxter, and P. Wilson: *J. Neut. Res.*, 2004, vol. 12 (1–3), pp. 21–25.
16. M. Preuss, P.J. Withers, and G. Baxter: *Mater. Sci. Eng., A*, 2006, vol. 437 (1), pp. 38–45.
17. J.W.L. Pang, M. Preuss, P.J. Withers, G. Baxter, and C. Small: *Mater. Sci. Eng., A*, 2003, vol. 356 (1–2), pp. 405–13.
18. P.J. Bouchard and P.J. Withers: *J. Neut. Res.*, 2004, vol. 12, pp. 39–44.
19. J.A. Francis, H.K.D.H. Bhadeshia, and P.J. Withers: *Mater. Sci. Technol.*, 2007, vol. 23 (9), pp. 1009–20.
20. *Aermet 100 Data Sheet*, Carpenter Technology Corporation, Wyomissing, PA, 09/01/1995.
21. R. Ayer and P.M. Machmeier: *Metall. Trans. A*, 1993, vol. 24A, pp. 1943–55.
22. M. Grujick: *Mater. Sci. Eng., A*, 1990, vol. 128, pp. 201–07.
23. G.R. Speich, D.S. Dabkowski, and L.F. Porter: *Metall. Trans. A*, 1973, vol. 4, pp. 303–15.
24. M.D. Perkas, P.L. Gruzin, A.F. Edneral, B.M. Mogutnov, Y.L. Rodionov, and M.A. Eremenko: *Mater. Sci. Heat Treat.*, 1985, vol. 27 (5), pp. 350–56.
25. A. Steuwer, J.R. Santisteban, M. Turski, P.J. Withers, and T. Buslaps: *Nucl. Instrum. Methods Phys. Res., Sect. B*, 2005, vol. 238 (1–4), pp. 200–04.
26. J. Altenkirch, A. Steuwer, M. Peel, D.G. Richards, and P.J. Withers: *Mater. Sci. Eng., A*, 2008, vol. 488 (1–2), pp. 16–24.
27. A.C. Larson and R.B. Von Dreele: Los Alamos National Laboratory Report No. LAUR 86-748, Los Alamos National Laboratory, Los Alamos, NM, 2000, <http://www.ncnr.nist.gov/xtal/software/gsas.html>.
28. B.H. Toby: *J. Appl. Crystallogr.*, 2001, vol. 34, pp. 210–13.
29. L. Edwards, P.J. Bouchard, M. Dutta, D.Q. Wang, J.R. Santisteban, S. Hiller, and M.E. Fitzpatrick: *Int. J. Press. Vess. Pip.*, 2005, vol. 82 (4), pp. 288–98.
30. T. Pirling, G. Bruno, and P.J. Withers: *Mater. Sci. Forum*, 2006, vols. 524–52, pp. 217–22.
31. A.P. Hammersley: “Fit2D: An Introduction and Overview”, Internal Report ESRF-97-HA02T, 1997, pp. 1–319, http://www.esrf.fr/computing/scientific/FIT2D/FIT2D_REF/fit2d_r.html.
32. “ASTM E 975-03: Standard Practice for X-Ray Determination of Retained Austenite in Steel with Near Random Crystallographic Orientation,” *Annual Book of ASTM Standards*, ASTM International, West Conshohocken, PA, 2003.
33. B.R. Kowalski: *Chemometrics, Mathematics and Statistics in Chemistry*, D. Reidel, Dordrecht, Holland, 1984.
34. I.C. Noyan and J.B. Cohen: *Residual Stress, Measurement by Diffraction and Interpretation*, Springer-Verlag, Berlin, 1987.
35. P.J. Withers, M. Preuss, A. Steuwer, and J.W.L. Pang: *J. Appl. Crystallogr.*, 2007, vol. 40 (5), pp. 891–904.
36. J.W.L. Pang, T.M. Holden, and T.E. Mason: *J. Strain Anal.*, 1998, vol. 33 (5), pp. 373–83.
37. J.F. Breedis and W.D. Robertson: *Acta Metall.*, 1963, vol. 11, pp. 547–59.